CONF-910318--12

COMPUTATIONAL MODELING OF GTA WELDING WITH EMPHASIS ON SURFACE TENSION EFFECTS*

T. Zacharia and S. A. David

Metals and Ceramics Division
Oak Ridge National Laboratory
Oak Ridge, TN 37831

CONF-910318--12

DE91 004771

1 ABSTRACT

A computational study of the convective heat transfer in the weld pool during gas tungsten arc (GTA) welding of Type 304 stainless steel is presented. The solution of the transport equations is based on a control volume approach which utilizes directly, the integral form of the governing equations. The computational model considers buoyancy and electromagnetic and surface tension forces in the solution of convective heat transfer in the weld pool. In addition, the model treats the weld pool surface as a deformable free surface. The computational model includes weld metal vaporization and temperature dependent thermophysical properties. The results indicate that consideration of weld pool vaporization effects and temperature dependent thermophysical properties significantly influence the weld model predictions. Theoretical predictions of the weld pool surface temperature distributions and the cross-sectional weld pool size and shape were compared with corresponding experimental measurements. Comparison of the theoretically predicted and the experimentally obtained surface temperature profiles indicated agreement within ± 8%. The predicted weld cross-section profiles were found to agree very well with actual weld cross-sections for the best theoretical models.

* To be published in the proceedings of the 3rd ASME-JSME Thermal Engineering Joint Conference, March 17-22, 1991.

Nomenclature

a_i	= activity
A, A_{srf}	= area
A_g, A_v	= constants
$\vec{B}$	= magnetic field
c_v	= specific heat
C_{liq}	= liquid mass fraction
C_{sol}	= solid mass fraction
D_{liq}	= depth of the weld pool
E	= arc voltage
f_{den}	= buoyancy force
f_{mhd}	= electromagnetic force
$\vec{g}, g_a$	= gravitational constant
h	= surface elevation
h_c	= convective heat transfer coefficient
ΔH°	= heat of adsorption
ΔH_v	= latent heat of vaporization
I	= arc current
$\vec{J}$	= electric current density
k_1	= constant related to the entropy of segregation
K	= adsorption coefficient
$\hat{n}$	= unit normal vector
p, p_{atm}, p_{srf}	= pressure
$\vec{q}_{arc}, \vec{q}_{evp}, \vec{q}_{srf}$	= heat transfer flux
r_b	= effective radius of heat flux
R	= gas constant
t	= time
T	= temperature
u, u_{sol}, u_{liq}	=internal energy
v	= volume
V	= velocity
W	= evaporation rate
α	= thermal expansion coefficient
β	= compressibility fraction
ϵ	= surface emmittance
η	= arc efficiency
Γ_s	= surface excess at saturation
γ, γ_m	= surface tension
κ	= thermal conductivity
μ	= viscosity of molten metal
ν	= kinematic viscosity
ρ	= density
ρ_o	= density at room temperature
σ	= Stefan-Boltzman constant
σ_n	= shear stress

2 INTRODUCTION

The development of the weld pool size and shape is influenced by the simultaneous occurrence of several important physical phenomena. These include the amount of heat transferred from the heat source to the workpiece, the fluid flow in the weld pool, and the accompanying convective heat transfer. Recent studies[1-11] have demonstrated that, in most cases, the convective heat transfer in the weld pool is controlled by the spatial variation of surface tension (surface tension gradient) that exists on the weld pool surface. The surface tension gradient arises from the spatial variation in surface temperature and the temperature dependence of surface tension. The spatial variation of surface tension causes the molten metal to be drawn along the surface from the region of lower surface tension to that of higher surface tension and this may result in very large surface flows. For pure metals and alloys the temperature coefficient of surface tension ($\frac{d\gamma}{dT}$) is negative. Thus, the surface tension is highest near the solid-liquid interface (lower temperature), causing the flow to be outward and away from the center of the pool. However, surface-active elements such as sulfur or oxygen can produce a positive $\frac{d\gamma}{dT}$ resulting in a higher surface tension at the center of the pool causing an inward flow.

The effect of surface-active elements has been investigated in detail by Heiple et al.[1,12-15] Their experiments indicate that surface-active elements significantly alter the surface tension of the weld metal thereby altering the flow field and associated convective heat transfer in the weld pool. Of particular significance is the reversal of flow which can occur in the presence of relatively small amounts of surface-active elements, causing a deep penetration. While the effect has been identified, the extent and the nature of the influence of surface-active elements on weld pool convective heat transfer and depth of penetration remain to be clarified. Prior modeling efforts[3-11] aimed at understanding surface tension gradient driven flow in the presence of surface-active elements considered a specified constant positive $\frac{d\gamma}{dT}$ which cannot be justified based on the physical phenomena governing the process. Furthermore, the available mathematical models include certain assumptions which cannot be justified on the basis of the actual physical conditions. These assumptions include constant thermophysical properties and exclusion of surface evaporation.

3 COMPUTATIONAL MODEL

Figure 1 shows the schematic drawing of the GTA welding process. As a result of the energy transfer between the arc and the metal surface a molten pool is formed, that subsequently grows due to combined conduction and convection heat transfer. We are concerned with the transient development of this molten metal pool due to the welding arc. Therefore, any computational model attempting to simulate the welding process should address the relevant factors that govern the development of this pool, i.e., 1) heat transfer from the arc to the metal surface, 2) coupled conduction and convection heat transfer, 3) phase transformation 5) weld pool evaporation 6) convection and radiation heat transfer between the specimen and the atmosphere, 7) accurate thermophysical properties for the metal.

The following assumptions were made in the present analysis:

1. The fluid flow and heat transfer inside the molten pool are adequately described by a two-dimensional, axi-symmetric representation.
2. The power distribution of the heat source is considered as Gaussian, based on available literature.

The computational model considers the densimetric coupling associated with the variation of density of the liquid metal in the formulation of all the transportive terms of the governing equations. Local density ρ of the liquid metal is considered in terms of a constant reference value ρ_o and the generalized compressibility fraction β, which represents the percentage density variation, i.e.

$$\rho = \rho_o(1 + \frac{\Delta\rho}{\rho_o}) = \rho_o(1 + \beta), \tag{1a}$$

$$\beta = \beta(T) = \frac{\Delta\rho}{\rho_o}(T). \tag{1b}$$

The equations that describe the transient development of the weld pool due to the coupled conduction and convection heat transfer are:

3.1 Governing Equations

The definition of all the symbols are presented in the appendix.

Conservation of mass

$$\frac{\partial}{\partial t}\iiint_V (1+\beta)\,dv + \iint_A (1+\tilde{\beta})\,\vec{V}\cdot\hat{n}\,dA = 0, \tag{2}$$

Conservation of momentum

$$\begin{aligned}\frac{\partial}{\partial t}\iiint_V (1+\beta)\,\vec{V}\,dv + \iint_A (1+\tilde{\beta})\,\tilde{V}\,\vec{V}\cdot\hat{n}\,dA \\ = \iint_A (p/\rho_o)(-\hat{n})\cdot\hat{u}dA + \iint_A (\sigma_n/\rho_o)\,dA \\ + \iiint_V \vec{f}_{den}/\rho_o\,dv + \iiint_V (\vec{f}_{mhd}/\rho_o)\,dv,\end{aligned} \tag{3}$$

where, the driving force for thermally driven flow in the weld pool is given by,

$$\vec{f}_{den} = \rho_o\,\vec{g}\,(1+\beta) \tag{3a}$$

and the electromagnetic body force is given by,

$$\vec{f}_{mhd} = \vec{J}\times\vec{B}. \tag{3b}$$

Conservation of energy

$$\begin{aligned}\frac{\partial}{\partial t}\iiint_V (1+\beta)[(1-C_{liq})\,u_{sol} + C_{liq}\,u_{liq}]\,dv \\ + \iint_A (1+\tilde{\beta})[(1-C_{liq})\,\tilde{u}_{sol} + C_{liq}\,\tilde{u}_{liq}]\,\vec{V}\cdot\hat{n}\,dA \\ = \iint_{A_{srf}} (\vec{q}_{arc}/\rho_o)\cdot(-\hat{n})dA + \iint_{A_{srf}} (\vec{q}_{evp}/\rho_o)\cdot(-\hat{n})dA + \iint_{A_{srf}} (\vec{q}_{srf}/\rho_o)\cdot(-\hat{n})dA.\end{aligned} \tag{4}$$

3.2 Boundary Conditions

The model considers the heat flux from the arc to the top surface of the metal as a specified radially symmetric Gaussian distribution given by,

$$\vec{q}_{arc} = \frac{3\eta EI}{\pi r_b^2}\cdot e^{-\left(\frac{3(x^2+y^2)}{r_b^2}\right)}. \tag{5}$$

The evaporation heat flux is calculated based on an overall vaporization model[16] given by,

$$\vec{q}_{evp} = W\Delta H_v \tag{6}$$

where ΔH_v is the heat of evaporation. The equation given by Dushman[17],

$$\log W = A_v + \log p_{atm} - 0.5 \log T \tag{6a}$$

was used to calculate the evaporation rate. The data reported by Kim[18] for the vapor pressure for stainless steel,

$$\log p_{atm} = 6.1210 - \frac{18836.}{T}, \tag{6b}$$

was used in the calculation. The values of H_v and A_v in equation 6 were estimated from the values given in Table 1[17,18] for the major constituents in the Type 304 stainless steel used in the study.

Table 1 Values for A_v and H_v

	A_v	H_v (kJ/kg)
Iron	2.52	6259.5
Nickel	2.531	6307.
Chromium	2.505	6622.5
Manganese	2.517	4112.6

At the surface of the specimen, the thermal boundary conditions for the atmospheric cooling is formulated in terms of the convective heat transfer and the radiative heat transfer and is given by,

$$\vec{q}_{srf} = h_c(T - T_a) + \sigma\epsilon(T^4 - T_a^4) \tag{7}$$

where, h_c is the heat transfer coefficient at the metal surface-atmosphere interface, T_a is the atmospheric temperature, σ is the Stefan-Boltzmann constant and ϵ is the surface emittance.

At the surface of the weld pool, the spatial variation of surface tension must be balanced by fluid shear since the surface must be continuous. Therefore, the shear stress at the surface is equated to the gradient of surface tension.

The surface shear stress components are formulated as,

$$\mu \frac{\partial V_x}{\partial z} = -\frac{\partial T}{\partial x}\frac{\partial \gamma}{\partial T}. \tag{8}$$

Surface tension is a strong function of temperature and composition. Experimental surface tension data are seldom available for any material throughout the temperature range of interest. In the calculations presented here surface tension was calculated as a function of temperature and activity for the entire temperature range of interest. The relation between surface tension of the solution and the temperature is given by[19]:

$$\gamma(T) = \gamma_m - A_g(T - T_m) - RT\Gamma_s \ln[1 + Ka_i], \tag{9a}$$

$$K = k_1 \exp(\frac{-\Delta H^\circ}{RT}), \tag{9b}$$

where γ is the surface tension of the solution at the temperature T, γ_m is the surface tension of the pure metal at the melting point T_m, R is the gas constant, Γ_s is the surface excess at saturation, K is the adsorption coefficient, k_1 is a constant which is related to the entropy of segregation, and ΔH° is the standard heat of adsorption, and a_i is the activity of the species i in solution.

Along the solid-liquid interface, the conventional no-slip conditions for a viscous fluid was assumed.

The computational model utilizes an explicit time-splitting numerical integration algorithm for the solutions of the governing equations.[20] The stability of the numerical scheme can be guaranteed by selecting a time step such that, all stability criteria[20] can be simultaneously satisfied. The selected time step must satisfy the Courant-Friedrichs-Lewy (CFL) criterion for free surface flows, the Courant criterion, based on maximum speed of flow in the weld pool, and the Neumann criterion, based on maximum momentum, thermal and mass diffusivity in the melt and in the solid. It is important to note that the maximum allowable time step cannot be accurately estimated *a priori*, since the maximum melt depth and the maximum velocities can change rapidly during the numerical integration. Therefore, the numerical solution requires the systematic consideration of the stability criteria at selected intervals during the numerical integration process.

4 RESULTS

Extensive testing was carried out to verify the predictions of the model described above by comparing the simulations with the results of an experimental study. Table 2. lists the numerical run conditions for the GTA welding of 4 x 4 x 1 cm Type 304 stainless steel specimens. The parameters were chosen such that the predictions of the model could be correlated with the results of an earlier experimental investigation[21] of the weld pool surface temperatures during spot gas tungsten arc welding of Type 304 stainless steel. In this paper, theoretical predictions of the weld pool surface temperatures and the weld pool size and shape, are compared with corresponding experimental measurements.

Table 2 Numerical Run Conditions

Case	Current Amps.	Voltage Volts.	Efficiency η	$\frac{d\gamma}{dT}$
1	50	10.1	0.8	Eq.(6)
2	100	13.2	0.8	Eq.(6)
3	150	15.1	0.8	Eq.(6)
4	100	13.2	0.8	-0.35×10^{-4}
5	150	15.1	0.8	-0.35×10^{-4}

Table 3. summarizes the experimental and numerical results obtained for the stationary welds made on Type 304 stainless steel. As expected, both the computational as well as the experimental study indicate that the weld pool peak temperature increases with increase in welding current for the three cases considered here. The peak weld pool temperature, obtained numerically, ranged from 1810 to 2380°C for the conditions investigated. These values for peak temperatures, even though slightly lower, compare well with the values obtained experimentally for the same welding conditions. The calculated lower peak temperatures are attributed to the vaporization theory based model (equation 6) that results in 10 % of the workpiece input energy going into metal vaporization. Actual vaporization losses are probably between 1 to 10 %. On the other hand, if the evaporation heat flux is not considered, the predicted weld pool surface temperatures would be considerably higher and may equal the boiling point of the material.

Table 3 Summary of Results

Case	Peak Temperature Experimental/Predicted [°C]	Weld Diameter Experimental/Predicted [mm]	Weld Depth Experimental/Predicted [mm]
1	1947. / 1810.	3.0 / 3.1	0.66 / 0.6
2	2160. / 2050.	5.8 / 5.7	2.4 / 2.7
3	2426. / 2380.	8.8 / 6.7	4.4 / 4.0
4	2160. / 2090.	5.8 / 5.8	2.4 / 2.6
5	2426. / 2570.	8.8 / 8.1	4.4 / 3.8

For example, figure 2 shows the peak weld pool temperature under the arc, with and without vaporization effects, as a function of weld duration. The results indicate that when weld pool evaporation is taken into account, the peak weld pool temperature increases monotonically with time until a maximum value, which is limited by the vaporization heat flux, is reached. It is interesting to note that for stainless steel, the peak temperature under the arc does not exceed a maximum value of approximately 2575°C. This is consistent with the work of Eagar et al.[22] who showed that, for steels, the heat loss due to metal vaporization places an upper limit on the temperature of arc weld pools. They estimated the maximum temperature to be approximately 2500°C. Recent, experimental work[21] on measuring the weld pool surface temperatures have shown that the maximum temperature during stationary GTA welding is closer to 2575°C. On the other hand, the results indicate that in the absence of vaporization the peak weld pool quickly reaches the boiling temperature. Clearly, the predicted as well as the experimentally obtained peak temperatures in Table 3 are well below the boiling temperature.

The weld pool surface temperature distributions for the cases 1-3 are presented in figure 3. Overall, the weld pool surface temperatures follow the expected Gaussian distribution. For the case of 50A and 100A, the predicted surface temperature profiles, though lower, compare favorably with actual experimental observations. It is interesting to note that the temperature profiles for case 2 (100A) have a shoulder which was presumed to indicate multiple cells in the flow field[21], which may be similar to Bernard cells. Bernard cells are primarily driven by surface tension in the presence of buoyancy force effects. In the present case, where a strong electromagnetic force is present, the exact mechanism of the break of the flow pattern into the multiple cells is not known. Such complex flow fields are believed to result in complex temperature distributions within the weld pool and may significantly influence the development of the weld pool as well as the solidification structure.

From figure 3, for the case of 150 A, the calculated temperature profile does not agree very well with experimental observations. In addition, the calculated temperature profile exhibits characteristics that are completely opposite to that experimentally observed. For example, at locations where the experimentally observed temperature profile shows an outward deviation from the ideal Gaussian profile, the calculated profile deviates inwardly. Since the spatial variation of surface tension is the predominant driving force that controls the convective heat transfer in the weld pool, it is likely that the surface tension behavior may have changed at the higher energy level and the associated higher temperatures.

Based on experimental observations during weld pool surface temperature measurements, Kraus[21] had reported an outward flow, implying a negative $\frac{d\gamma}{dT}$ at the weld pool surface, at the higher current and temperatures levels. The Type 304 stainless steel considered in this investigation contains 220 ppm sulfur, which is reported[24] to produce a positive surface tension gradient at the weld pool surface. In order to obtain a clear understanding of the surface tension behavior during welding and its effect on weld penetration, especially during high current welding, the calculations

for 100A and 150A welding current (cases 4-5) were repeated for a constant $\frac{d\gamma}{dT}$ of -0.35×10^{-4} . The resulting surface temperature distributions are compared with experimental values, in figure 4, indicating very good agreement.

The results of the present study suggest that the surface tension model (equation 6) used in the analysis may not be valid at high temperatures and long arc/metal interaction times. This should not be surprising since the formalism describing the surface tension behavior was developed for a binary Fe-S system in the absence of arc plasma. Since the weld pool surface is exposed to the arc plasma for a long time during welding, the chemical nature of the surface may become significantly different.

The results of the weld pool width and depth of penetration are also presented in Table 3. The depth to width ratios obtained in this study are somewhat lower than those obtained earlier for moving arc welds. This is consistent with the results of a recent study of weld penetration during stationary GTA welding[25,26] on another heat of Type 304 stainless steel. The lower depth to width ratios during stationary welding were attributed to higher surface temperatures which could result in a negative $\frac{d\gamma}{dT}$ on the weld pool surface and an outward flow. Indeed, this appears to be the case for the welds made at higher welding currents, as the data of Table 3 reveal. Comparison of the calculated and experimentally obtained results indicates good agreement.

The experimental and predicted results of the weld pool cross sectional shape and size are compared in Figs. 5, 6 and 7. For a welding current of 50A, the results show a relatively shallow weld with a depth to width ratio of 0.25. The calculated as well as the experimentally observed depth to width ratio is appreciably lower than the values reported in literature for Type 304 stainless steels with comparable sulfur levels[12-15]. For the case of 100 A (see figure 6), the shape of the weld puddle is markedly different, with a considerable increase in depth of penetration. The transverse section of the weld indicates a somewhat cylindrical shaped weld pool. The weld depth/width ratio in this case is 0.39.

The experimental and predicted cross-sectional shape and size for 150A welding current (case 5) is compared in figure 7. As would be expected, the calculated shape of the weld pool is different from the welds made at 50A and 100A welding current. Examination of the results indicate that the calculated weld geometry using a constant negative $\frac{d\gamma}{dT}$ agrees best with the actual observations.

5 CONCLUSIONS

A systematic study was carried out to verify the predictions of a transient multi-dimensional computational model by comparing the simulations with the results of an experimental study. The welding parameters were chosen such that the predictions of the model could be correlated with the results of an earlier experimental investigation. Theoretical predictions of the weld pool surface temperature distributions, the weld pool size and the shape were compared with corresponding experimental measurements.

Overall, the predictions of the model compared favorably with actual experimental observations. The effect of sulfur on the convective heat transfer in the weld pool was modeled by considering $\frac{d\gamma}{dT}$ as a function of temperature and sulfur content. The results indicate that the surface tension behavior may change at the higher energy level (near 100 A) and the associated higher surface temperatures.

The results also showed that vaporization places an upper limit on the maximum weld pool temperature, which for stainless steel is approximately 2575°C. This is comparable to earlier experimental, as well as theoretical, predictions. If vaporization effects are not considered in the analysis, the weld pool quickly reaches the boiling temperature, which for stainless steel is 2808°C.

6 ACKNOWLEDGEMENTS

The authors would like to thank J. C. Whitson for reviewing the manuscript. The research

was sponsored by the Division of Materials Sciences, U. S. Department of Energy, under contract DE- AC05-84OR21400 with Martin Marietta Energy Systems, Inc.

7 REFERENCES

1. C. R. Heiple and J. R. Roper. 1982. Mechanism for minor element effect on GTA fusion zone geometry. *Welding Journal.* Vol. 61(4), p. 97s.
2. N. S. Tsai, and T. W. Eagar. 1984. Modeling of Casting and Welding Process II, p. 317.
3. D. R. Athey. 1980. A mathematical model for fluid flow phenomena in weld pools. *Journal of Fluid Mechanics.* Vol. 98, p. 787.
4. G. M. Oreper and J. Szekely. 1984. Heat and fluid flow phenomena in weld pools. *Journal of Fluid Mechanics.* Vol. 147, p. 53.
5. C. Chan, J. Mazumder, and M. M. Chen. 1984. A two-dimensional transient model for convection in laser melted pools. *Metall. Trans.* Vol. 15A, p. 2175.
6. S. Kou and D. K. Sun. 1985. Fluid flow and weld penetration in stationary arc welds. *Metall. Trans.* Vol. 16A, p. 203.
7. S. Kou and Y. H. Wang. 1986. Weld pool convection and its effect. *Welding Journal.* Vol. 65(3), p. 63s.
8. T. Zacharia, S. A. David, J. M. Vitek and T. DebRoy. 1989. Heat Transfer During Nd:Yag Pulsed Laser Welding and Its Effect on Solidification Structure of Austenitic Stainless Steels. *Metallurgical Transactions.* Vol. 20A, p. 1125.
9. R. E. Sundell, S. M. Correa, L. P. Harris, H. D. Solomon, L. A. Wojcik, W. F. Savage, D. W. Walsh and G-D. Lo. 1986. Minor element effects on gas tungsten arc weld penetration. GE Report No. 86SRD013, Schenectady, New York.
10. T. Zacharia, A. H. Eraslan, and D. K. Aidun. 1988. Modeling of non-autogenous welding. *Welding Journal.* Vol. 67(1), p. 18s.
11. T. Zacharia, A. H. Eraslan, and D. K. Aidun. 1988. Modeling of autogenous welding. *Welding Journal.* Vol. 67(3), p. 53s.
12. C. R. Heiple, J. R. Roper, R. T. Stagner and J. J. Alden. 1983. Surface active element effects on the shape of GTA, laser and electron beam welds. *Welding Journal.* Vol. 62(3), p. 72s.
13. C. R. Heiple and J. R. Roper. 1981. Effect of Selenium on GTAW fusion zone geometry. *Welding Journal.* Vol. 60(8), p. 143s.
14. C. R. Heiple and P. Burgardt. 1985. Effects of SO_2 shielding gas additions on GTA weld shape. *Welding Journal.* Vol. 64(6), p. 159s.
15. C. R. Heiple and J. R. Roper. 1981. Effects of minor elements on GTAW fusion zone shape. Trends in Welding in the United States, Ed. S. A. David, American Society for Metals, Metals Park, Ohio. p. 489.
16. M. Choi, R. Grief and M. Salcuden. 1987. Numerical Heat Transfer, Vol. 11, p. 477.
17. S. Dushman. 1962. Scientific Foundations of Vacuum Technique, John Wiley and Sons, New York.
18. Kim, C. S. 1975. Thermophysical Properties of Stainless Steels, Argonne National Laboratory, Report No. ANL-75-55.
19. P. Sahoo, T. DebRoy, and M. J. McNallan. 1988. Surface tension of binary metal- surface active solute systems under conditions relevent to welding metallurgy. *Metall. Trans.* Vol. 19B, p. 483.
20. T. Zacharia, A. H. Eraslan, D. K. Aidun, and S. A. David. 1989. Three dimensional transient model for arc welding process, *Metallurgical Transactions B.*, Vol. 20B: p. 645.
21. Kraus, H. G. 1989. Welding Journal, Vol. 68(7), p. 269s.
22. Block-Bolten, A., and Eagar, T. W., 1984. Metall. Trans. B, Vol. 15B(9), p. 461.

23. T. Zacharia, S. A. David and J. M. Vitek. Computational modeling of stationary weld pool and comparison to stainless steel 304 experimental results. accepted for publication in *Metallurgical Transactioins B.*
24. B. J. Keene, K. C. Mills, J. W. Bryant, and E. D. Hondros. 1982. Effects of Interaction Between Surface Active Elements of the Surface Tension of Iron, Canadian Metallurgical Quarterly, Vol. 21: p. 393.
25. T. Zacharia, S. A. David, J. M. Vitek and T. DebRoy. Weld Pool Development During GTA and Laser Welding of Type 304 Stainless Steel. Part I - Theoretical Analysis. *Welding Journal.* Vol. 68(12). p. 499s.
26. T. Zacharia, S. A. David, J. M. Vitek and T. DebRoy. Weld Pool Development During GTA and Laser Welding of Type 304 Stainless Steel. Part II - Experimental Correlation. *Welding Journal.* Vol. 68(12). p. 510s.

ORNL-DWG 87-19277R

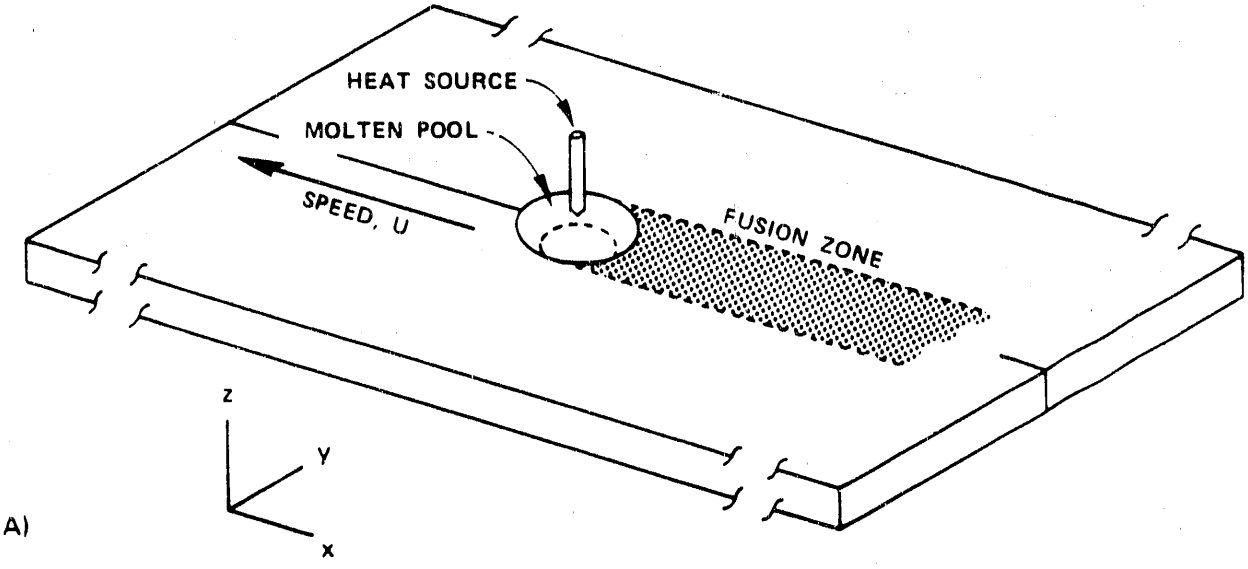

A)

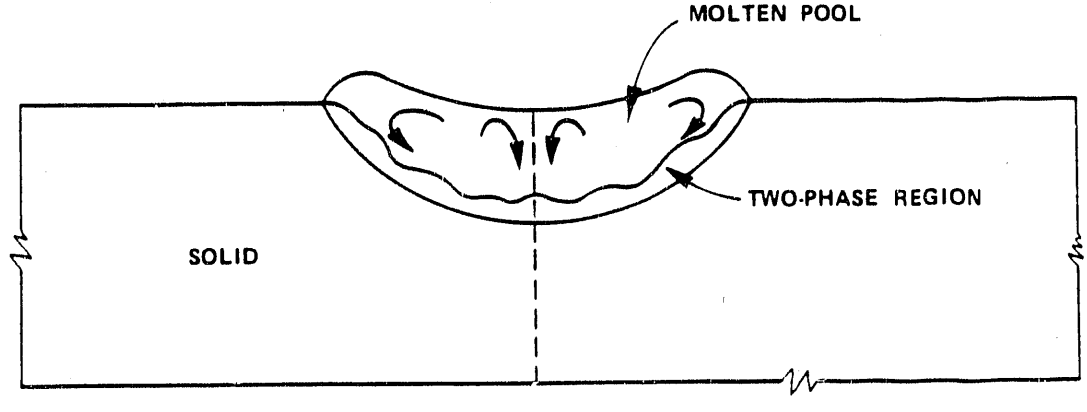

B)

ORNL-DWG 90-10218

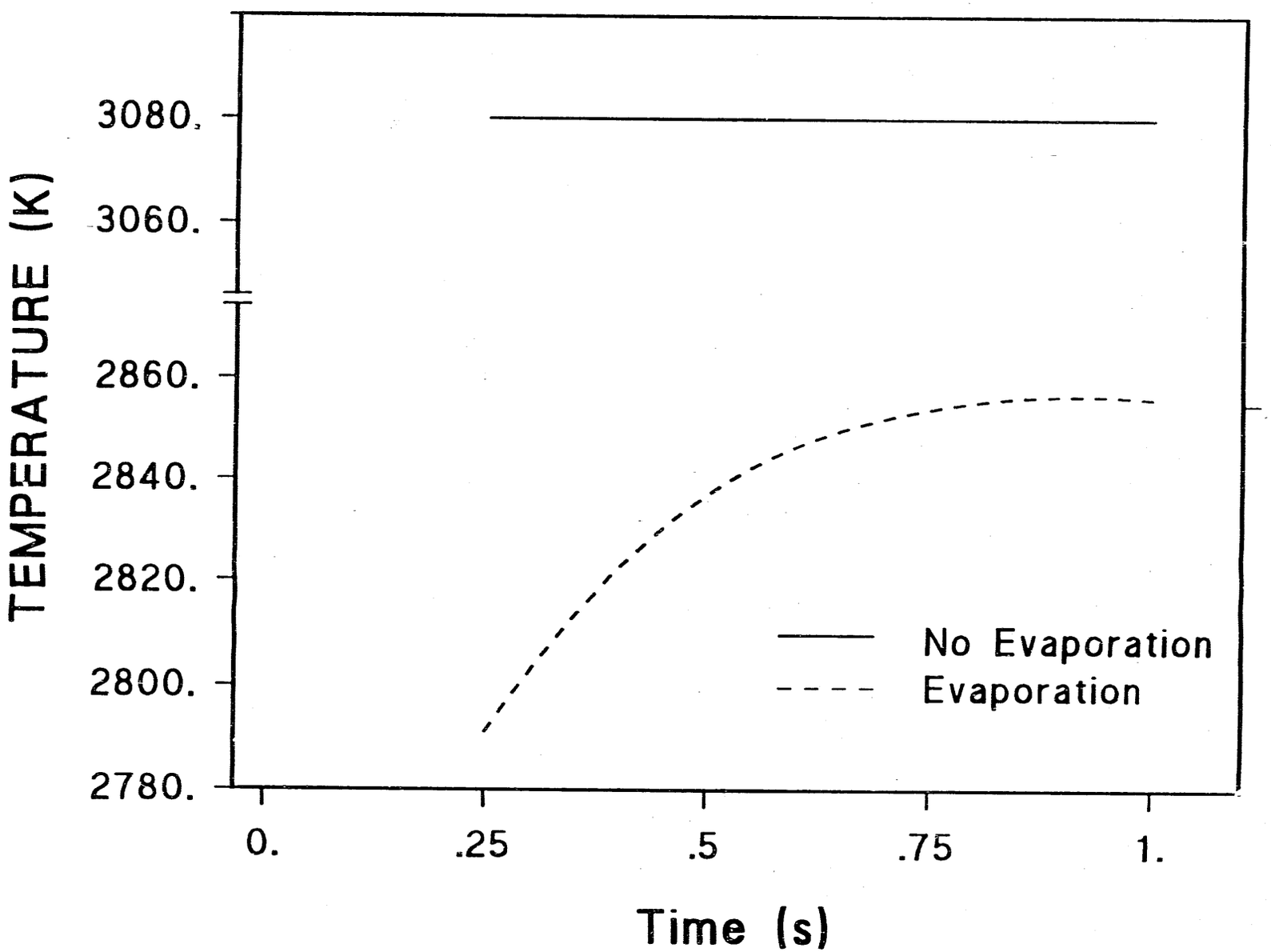

ORNL-DWG 90-8325R

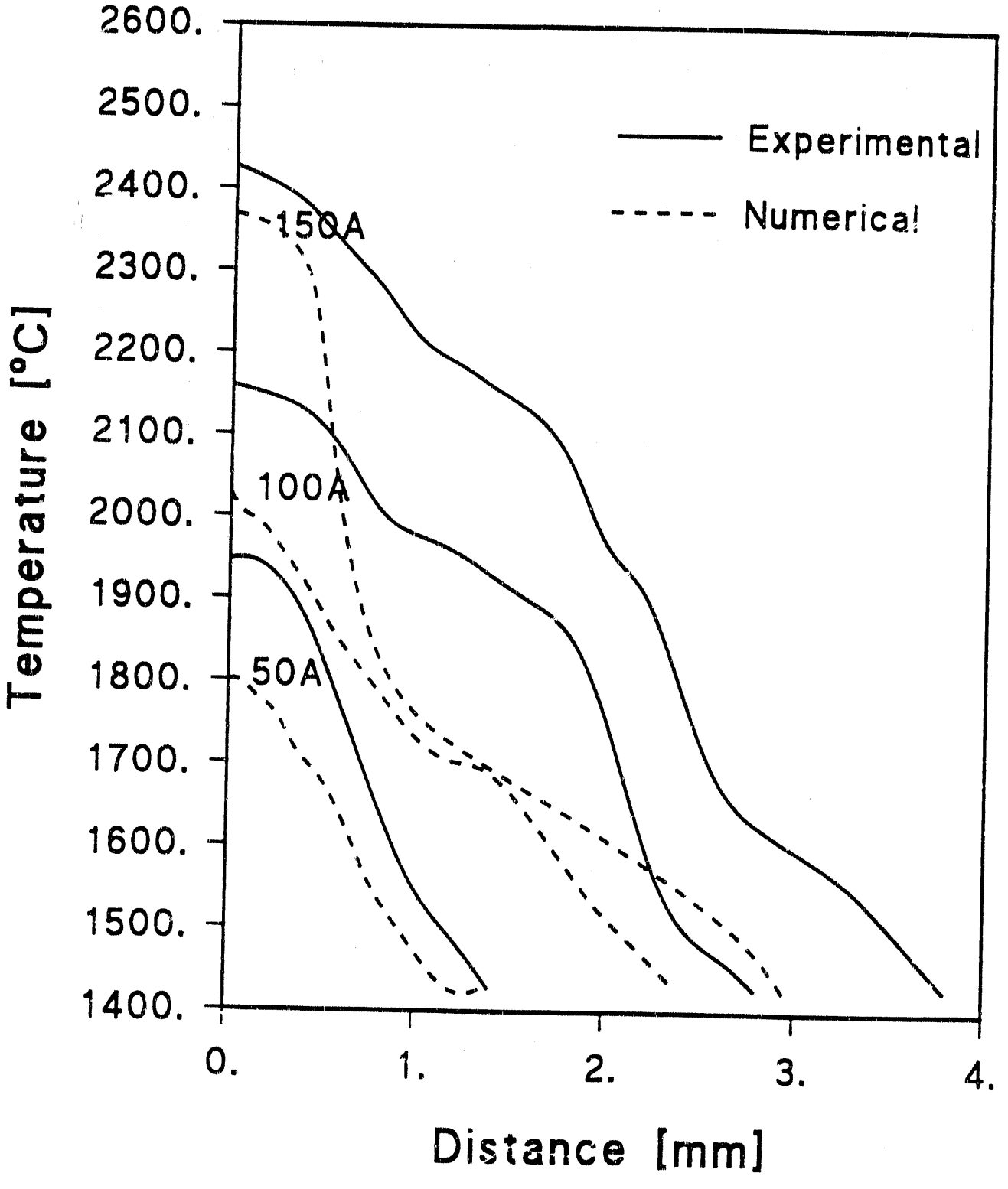

ORNL-DWG 90-8325R

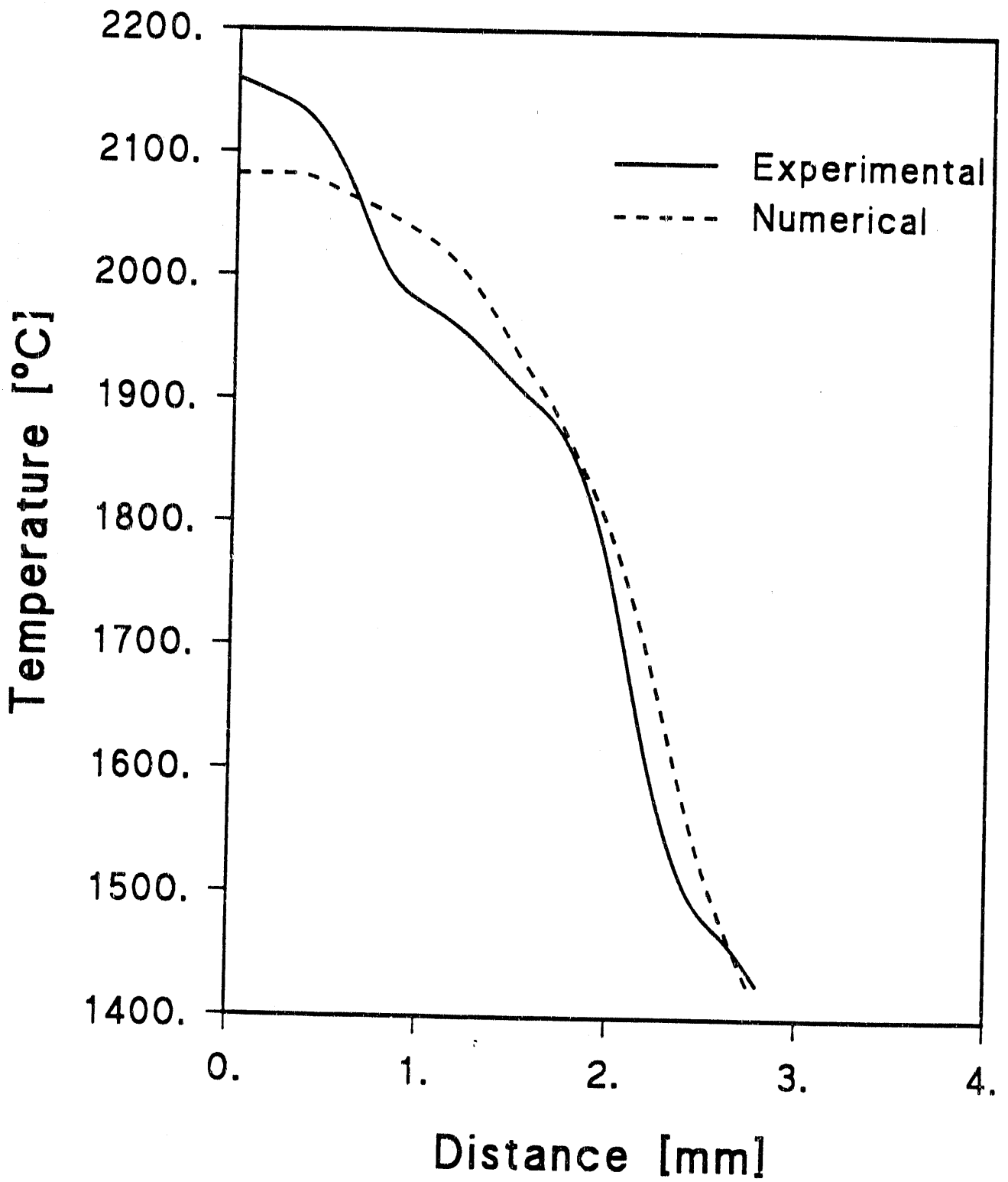

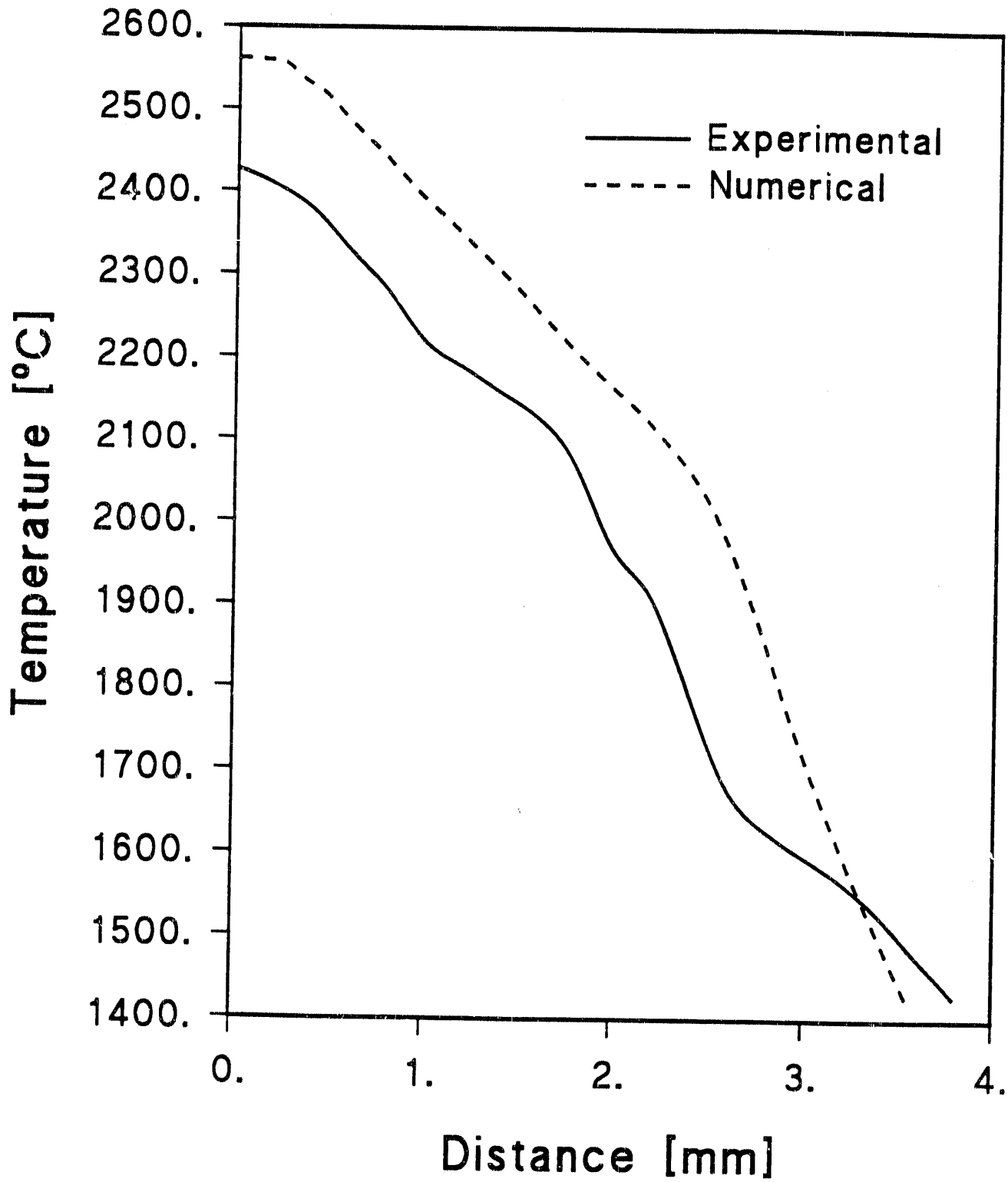
2600.
2500.
2400.
2300.
2200.
2100.
2000.
1900.
1800.
1700.
1600.
1500.
1400.
Temperature [°C]
Experimental
Numerical
0.
1.
2.
3.
4.
Distance [mm]

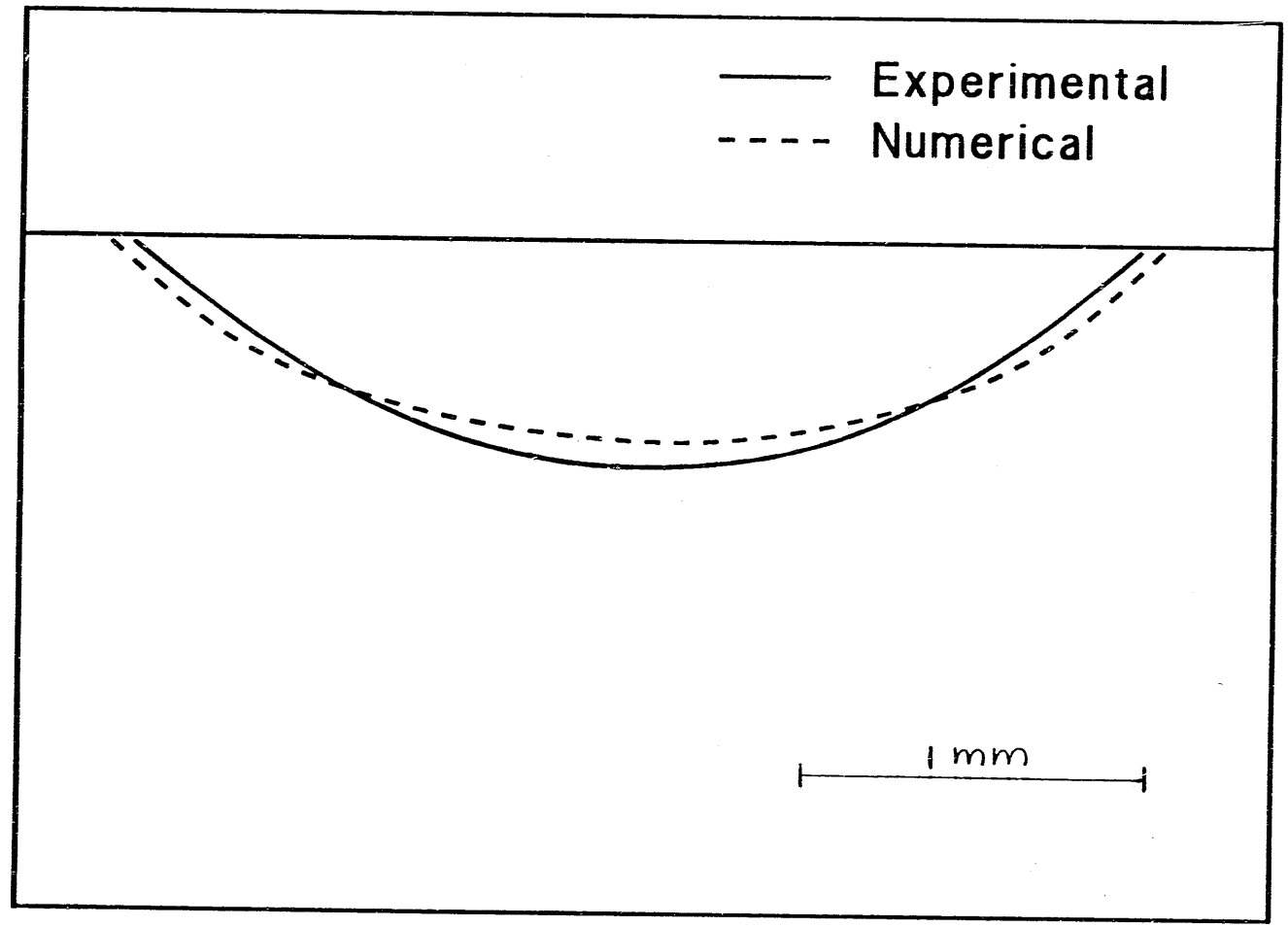
Experimental
Numerical
1 mm

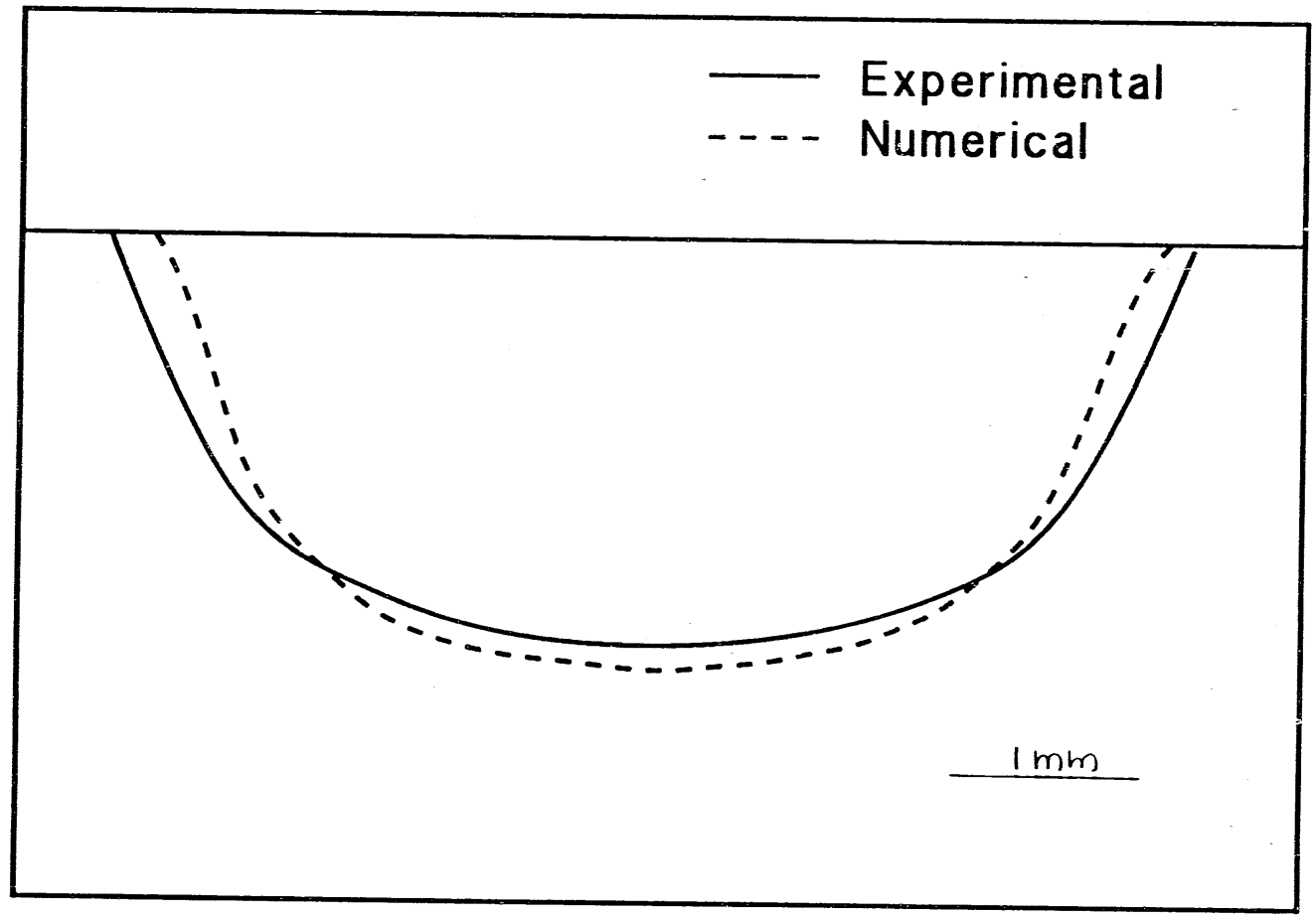
Experimental
Numerical
1mm

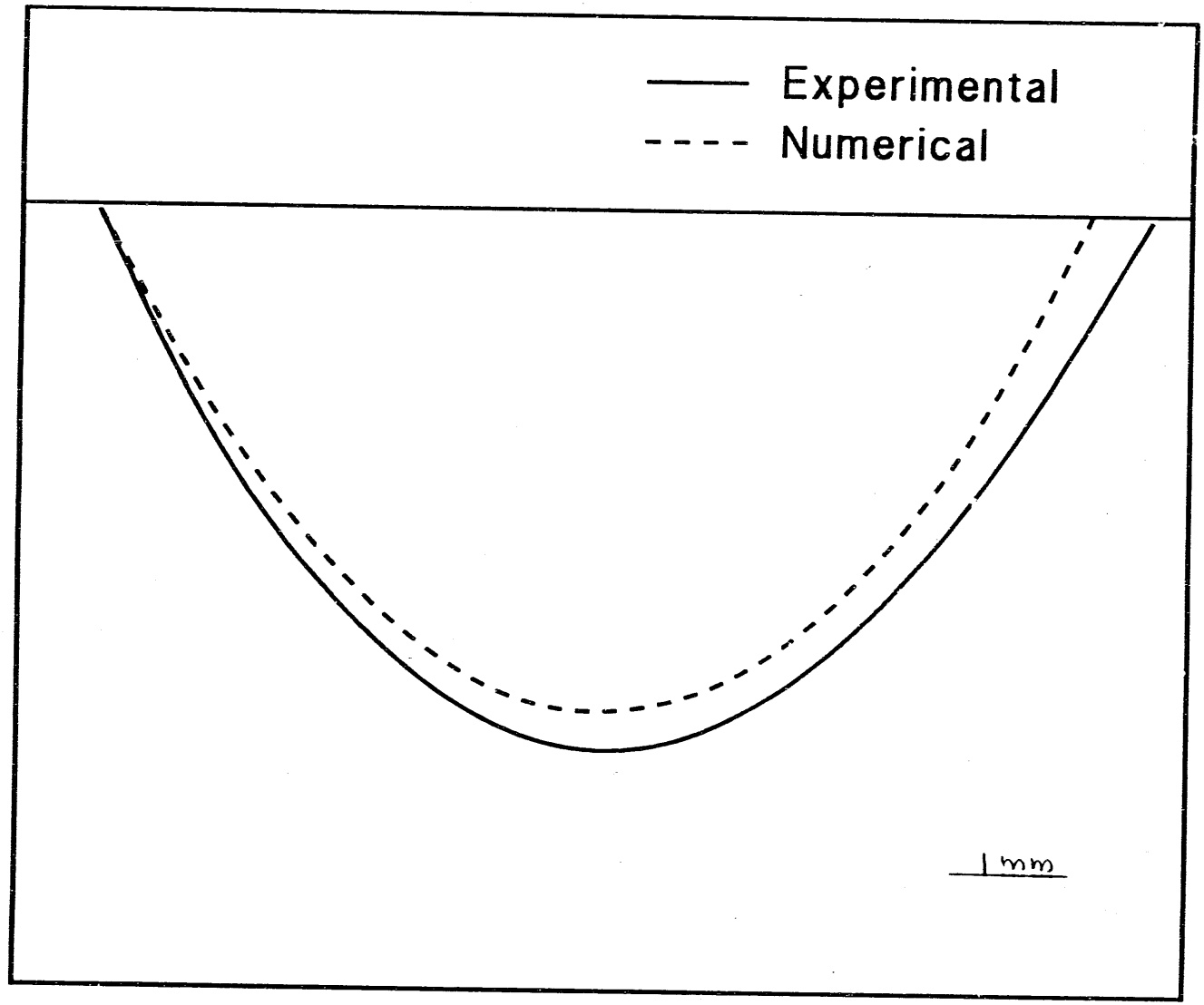
Experimental
Numerical
1 mm

END

DATE FILMED

02 / 05 / 91